SAND2000-1748C

AIAA 2000-2550

Verification and Validation for Laminar Hypersonic Flowfields

Christopher J. Roy, Mary A. McWherter-Payne,
and William L. Oberkampf
Sandia National Laboratories
Albuquerque, NM

Fluids 2000
19-22 June 2000 / Denver, CO

AIAA-2000-2550

VERIFICATION AND VALIDATION FOR LAMINAR HYPERSONIC FLOWFIELDS

Christopher J. Roy,[‡] Mary A. McWherter-Payne,[†] and William L. Oberkampf[§]

Sandia National Laboratories*

P. O. Box 5800

Albuquerque, NM 87185

Abstract

The accuracy of Mach 8 laminar flow solutions over a spherically-blunted cone is verified, and the various physical models are validated. Verification of the solution accuracy is demonstrated by monitoring iterative convergence, performing a comprehensive grid convergence study, comparison to benchmark inviscid results, and code-to-code comparisons. Although the numerical scheme is nominally second order accurate in space, the presence of first order accuracy at the shock discontinuity results in first order behavior for the surface pressure distributions as the grid is sufficiently refined. Alternative methods are proposed for analyzing the spatial convergence behavior and determining the order of accuracy for mixed first and second order schemes. Validation of the computational model is performed via surface pressure comparisons with high-quality experimental data. Careful attention is paid to the assumptions in the computational and experimental modeling. In particular, the thermodynamic state of the hypersonic wind tunnel nozzle is examined and arguments are made for the presence of a significant amount of thermal nonequilibrium. Bias errors in the experimental Mach number calibration are discussed which are related to the assumption of thermal equilibrium (-0.23%) and the averaging of probe data over the entire test section (+0.6%). Differences between the simulation results for surface pressure and the experimental data are found to be as large as 3.3%. These differences are well outside the experimental 2σ error bounds, even after accounting for the experimental bias errors.

Nomenclature

C_p	specific heat at constant pressure, $J/kg{\cdot}K$
e	specific internal energy, $J/kg{\cdot}K$
$\dot{e}$	specific internal energy rate of change, $J/kg{\cdot}K{\cdot}s$
f_k	solution variable on mesh level k
g_i	i^{th} order error term coefficient
h_k	grid spacing on mesh level k
k	thermal conductivity, $W/m{\cdot}K$
N_k	total number of mesh cells on grid level k
P	continuum breakdown parameter
Pr	Prandtl number (= 0.71)
p	pressure, N/m^2, or spatial order of accuracy
R	specific gas constant, $J/kg{\cdot}K$ ($R = R_u / W$)
R_N	nose radius (= 0.00508 m or 0.2 in)
R_u	universal gas constant (= $8314.34\ J/kmol{\cdot}K$)
r	grid refinement factor ($r = h_{k+1}/h_k$)
T	translational-rotational temperature, K
T_{vib}	vibrational temperature, K
W	molecular weight (= $28.013\ kg/kmol$ for N_2)
x	axial coordinates, m
y	radial coordinate (Cartesian for 3-D), m
z	Cartesian coordinate for 3-D, m
γ	ratio of specific heats ($\gamma = C_p/C_v$)
θ_{vib}	characteristic vibrational temperature, K
μ	absolute viscosity, $N{\cdot}s/m^2$
ρ	density, Kg/m^3
τ	characteristic vibrational relaxation time, s
ϕ	Landau-Teller acceleration factor ($\tau = \tau_{LT}/\phi$)

‡ Senior Member of Technical Staff, MS 0835, E-mail: cjroy@sandia.gov, Member AIAA

† Principle Member of Technical Staff, MS 0825, E-mail: mapayne@sandia.gov, Senior Member AIAA

§ Distinguished Member of Technical Staff, MS 0828, E-mail: wloberk@sandia.gov, Associate Fellow AIAA

* Sandia is a multiprogram laboratory operated by Sandia Corporation, a Lockheed Martin Company, for the United States Department of Energy under Contract DE-AC04-94AL85000.

DISCLAIMER

DISCLAIMER

Portions of this document may be illegible in electronic image products. Images are produced from the best available original document.

Subscripts and Superscripts

k	Mesh level
LT	Landau-Teller
RE	Richardson Extrapolation
*	equilibrium value

Introduction

With advances in computing power, engineers increasingly rely on modeling and simulation for the design and certification of engineering systems. Thus, there is a need to increase the confidence in these simulations, especially in high-risk areas such as civil aviation, nuclear power, and nuclear weapons systems. Verification and validation provides the primary means by which one can assess the accuracy of computational simulations.

In order to develop a computational model, one must first define a conceptual model of the physical system.[1] Verification is the process of determining that a model implementation accurately represents the developer's conceptual description and assessing how accurately this conceptual model is solved. Validation, as defined in Ref. 1, is "the process of determining the degree to which a model is an accurate representation of the real world from the perspective of the intended uses of the model." Simply put, verification asks the mathematical question "are we solving the equations right," while validation asks the physical question "are we solving the *right* equations."

Verification can be separated into two parts, code verification and solution verification. Code verification is used to find coding errors in the discrete solution to the chosen governing equations and boundary conditions. Code verification can be accomplished by comparison to analytical solutions, highly accurate benchmark solutions, and by the method of manufactured solutions.[2] The latter is an elegant method which includes the application of *a priori* analytical solutions to the governing equations with a subsequent generation of source terms. During this phase, the formal order of accuracy of the numerical scheme can also be verified with carefully chosen problems which do not require limiting procedures (e.g. flux limiting, realizeability limiting) and which have well-characterized boundary conditions. In this paper, code verification is addressed only through a comparison to highly accurate numerical results for inviscid flow and through a code-to-code comparison.

Solution verification (or solution accuracy assessment) is concerned with quantifying the computational error of a given numerical simulation and should ideally take place after code verification has been completed. The two main aspects of solution verification are iterative convergence and spatial, or grid, convergence. The former deals with the marching of a solution in pseudo-time towards a steady state or the use of sub-iterates to recover a time-accurate solution, while the latter deals with the adequacy of the mesh upon which the discrete equations are being solved. The spatial order of accuracy is also an important metric for assessing the errors due to spatial resolution. This paper places a strong emphasis on solution verification. In particular, issues dealing with the spatial accuracy of flows with discontinuities will be discussed.

Validation consists of comparing a verified numerical solution with high quality experimental data. Validation can be performed at both the submodel level (e.g. transport models, equation of state models, thermodynamic models, turbulence models) and at the system level through comparisons with high quality experimental data. Once model validation has been performed, conclusions can be drawn regarding the applicability of the proposed mathematical models and recommendations for improvements can be made.

The computational fluid dynamics code used in the current work is SACCARA, the Sandia Advanced Code for Compressible Aerothermodynamics Research and Analysis. The SACCARA code was developed from a parallel distributed memory version[3-6] of the INCA code,[7] originally developed by Amtec Engineering. This code has been developed to provide a unique, massively parallel, three-dimensional compressible fluid mechanics/aerothermodynamics analysis capability for transonic and hypersonic flight systems. Since testing, both flight and ground, has decreased in recent years due to rising costs, it is necessary for modeling and simulation to fill in the gap. Verification and validation of the computational techniques developed for design and analysis is critical to this process.

The current paper presents computational results for a Mach 8, laminar, spherically-blunted cone which was studied experimentally at the Sandia National Laboratory hypersonic wind tunnel facility. The model had a planar slice on the aft section (parallel to the longitudinal axis), where 10, 20, and 30 degree flaps could be mounted. The experimental database consists of both force and moment[8,9] and surface pressure[10,11] measurements.

The remainder of this paper is organized as follows. A brief discussion of the experimental setup is given, followed by the details of the computational tool including thermodynamic models. Comprehensive verification of the accuracy of the simulations is presented, including a discussion of the iterative and spatial accuracy. Model validation results are presented which include calculations of the hypersonic nozzle used to determine the state of the vibrational excitation at the test section. Results are then given which compare the verified simu-

lation distributions for surface pressure to experimental data. Finally, discrepancies between the experimental and computational results are addressed and conclusions are drawn.

Experimental Setup

The simulations presented herein are used to compare to surface pressure data collected under the Joint Computational/Experimental Aerodynamics Program (JCEAP) at the Sandia National Laboratories hypersonic wind tunnel facility.[10,11] The wind tunnel is a blow-down-to-vacuum configuration and has capabilities for Mach 5, 8, and 14 flow. The Mach 8 nozzle uses dry nitrogen (99.999% pure) with a series of heater screens upstream of the nozzle throat to prevent nitrogen condensation in the test section. The tunnel cross-section is rectangular (0.127 *m* x 0.178 *m*) in the plenum, and transitions to a circular cross-section approximately 0.1 *m* upstream of the nozzle throat.[8] The tunnel test section, located approximately 2 *m* downstream of the nozzle throat, has a diameter of 0.35 *m*.

The JCEAP model is a ten degree half-angle spherically blunted cone with a length of 0.2639 *m* and a nose radius of 0.00508 *m* (0.2 *in*). A planar slice is located on the aft section (beginning at 0.7 of the length of the body) where 10, 20, and 30 degree flaps can be mounted (see Fig. 1). The model contains a total of 96 pressure ports located circumferentially around the body at various axial stations, in addition to a number of ports on the slice and flaps. A large quantity of data was taken at various angles of attack, roll angles, and at two different axial locations in the tunnel. After varying these parameters and conducting a number of repeat runs, a statistical method was then used to greatly improve the estimate of experimental measurement uncertainty.[10,11]

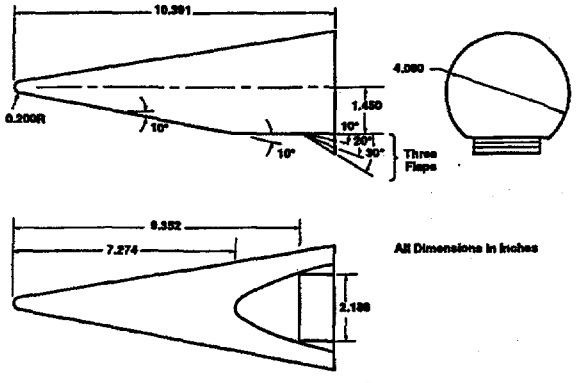

Fig. 1 JCEAP model geometry.

The experimental uncertainty comes from a number of sources including tunnel flow nonuniformity, model imperfections, positional uncertainty, instrumentation uncertainty, and run-to-run variations in freestream conditions.

The test conditions are given in Table 1 along with run-to-run variations for one standard deviation. The stagnation pressure is measured in the plenum, and the stagnation temperature is determined from the plenum pressure and a mass balance between the nozzle throat and a control valve located upstream of the heaters. The tunnel Mach number is calibrated by inserting a pitot pressure rake into the test section and then assuming thermal equilibrium and isentropic flow in the nozzle. The validity of this assumption will be assessed in the Model Validation section. The static pressure and Reynolds number are then calculated from the Mach number and stagnation values, again assuming thermal equilibrium.

Table 1 Test conditions for JCEAP surface pressure experiments

Flow Parameter	Mean Value	One Standard Deviation
Freestream Mach Number	7.841	0.032%
Stagnation Pressure	2.4724×10^6 *N/m*^{2}	2.1%
Stagnation Temperature	632.8 *K*	2.1%
Freestream Static Pressure	286.8 *N/m*^{2}	1.4%
Freestream Static Temperature	47.7 *K*	*none given*
Freestream Unit Reynolds Number	6.88×10^6/*m*	3.7%

Flowfield Model

The SACCARA code employs a massively parallel distributed memory architecture based on multi-block structured grids. The code is capable of simulating axisymmetric, two-dimensional, and three-dimensional flows using a cell-centered finite volume discretization. The solver is a Lower-Upper Symmetric Gauss-Seidel scheme based on the works of Yoon et al.[12,13] and Peery and Imlay,[14] which provides for excellent scalability up to thousands of processors.[15]

Results are presented for the laminar flow over the

JCEAP model geometry. Unless otherwise stated, all results presented herein use a second order Steger-Warming[16] flux scheme and assume perfect gas ($\gamma = 1.4$) flow of nitrogen. The boundary conditions are assumed to be fixed at the values reported in Table 1, and a constant wall temperature of 316.7 *K* was used as suggested in Ref. 17. The simulations were run using a single 400 MHz processor of a Sun Enterprise 10000 shared-memory machine unless otherwise noted. The solutions herein assume axisymmetric flow to reduce the computational effort, with the exception of a single three dimensional calculation performed to test this assumption. Comparisons with the JCEAP experimental data are thus limited to the data on the conical regions of the model only.

Governing Equations

The Navier-Stokes equations are solved for conservation of mass, momentum, and energy. The SACCARA code has two options for determining interface fluxes, the Steger-Warming[16] flux vector splitting scheme and Yee's[18] symmetric TVD scheme. Second order spatial accuracy is obtained with the former via MUSCL extrapolation, while the latter is nominally second order in smooth regions of the flow. Both schemes employ a flux limiter which reduces to first order spatial accuracy in regions with large second derivatives of pressure and temperature, and the effects of this limiting will be discussed in the Verification section. The viscous terms are discretized using central differences.

Thermodynamic Models

When applied to flows with a single chemical species, the SACCARA code has three options for the thermodynamic model: calorically perfect gas, thermally perfect gas in thermal equilibrium, and thermally perfect gas in thermal nonequilibrium.

Calorically Perfect Gas

For a calorically perfect gas, the specific heats are constant. The equation of state and energy-temperature relation are expressed as

$$p = \rho(\gamma - 1)e \tag{1}$$

and

$$T = (\gamma - 1)e/R, \tag{2}$$

respectively. For diatomic nitrogen below 300 *K*, the ratio of specific heats γ is 1.4. Thermally frozen flow can occur when the thermal relaxation time scales are much larger than the flow residence time scales, and may be observed in compressive flows such as shock waves at low pressures or in rapidly expanding flows. In a thermally frozen flow, the calorically perfect gas assumption is valid provided the correct value of gamma is employed ($\gamma = 1.4$ for linear, diatomic molecules).

Thermal Equilibrium

As the temperature increases, vibrational modes are excited and the equilibrium value of gamma will drop. This behavior is demonstrated in Fig. 2 for nitrogen, which has a characteristic vibrational temperature of 3390 *K*. For a thermally perfect gas in thermal equilibrium, the specific heats, enthalpy, and entropy are functions of temperature only. The SACCARA code uses polynomial curve-fits following the work of McBride et al.[19] For flows in thermal equilibrium, the thermal relaxation time scale is assumed to be much smaller than the flow residence time scale.

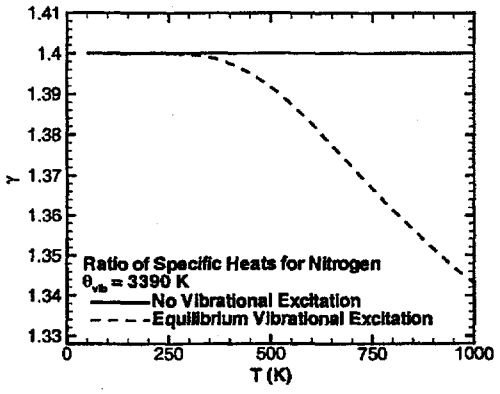

Fig. 2 Ratio of specific heats, γ, as a function of temperature for nitrogen.

Thermal Nonequilibrium

For a thermally perfect gas in thermal nonequilibrium, the thermal relaxation time scale is, in some region of the flow, of the same order of magnitude as the flow residence time scale. In order to predict flows with thermal nonequilibrium, a separate transport equation for the vibrational energy is solved.[20] The right-hand side (*RHS*) of the vibrational energy transport equation contains a source term of the Landau-Teller (L-T) form which governs the thermal relaxation process

$$RHS = \frac{e_{vib}^{*}(T) - e_{vib}(T_{vib})}{\tau_{LT}} \tag{3}$$

where the Landau-Teller relaxation time scale τ_{LT} is found from the correlation of *Millikan and White*.[21] This formulation is based on a harmonic oscillator model and assumes that the energy is distributed among the

vibrational energy levels according to a Boltzmann distribution.

While the standard L-T vibrational relaxation has been shown to give good agreement with experimental data for compressive flows, as early as the 1960's, researchers found evidence that vibrational de-excitation occurred much more rapidly for certain expanding flows than was predicted by L-T theory.[22] This accelerated relaxation rate is due to anharmonic effects and non-Boltzmann population distributions in the vibrational energy levels (often referred to as vibrational pumping), and can be expressed in terms of a local acceleration factor:

$$\phi = \dot{e}_{vib} / \dot{e}_{vib,LT} \qquad (4)$$

which multiplies the standard L-T relaxation rate.[23] Ruffin[24] suggests that ϕ is a function of the translational temperature T and the T_{vib}/T ratio only. If this assertion holds, then solutions for the case of thermal relaxation of a quiescent gas could be used to construct a correlation for $\phi = \phi(T, T_{vib}/T)$ which in turn could provide a relatively simple correction to the standard L-T formulation. Fig. 3 shows the behavior of the L-T acceleration factor as a function of the T_{vib}/T ratio for three different translational-rotational temperatures. The correction factor is near unity for compressive flows ($T > T_{vib}$) and grows as the T_{vib}/T ratio increases. This information will be used in the validation of the thermodynamic model.

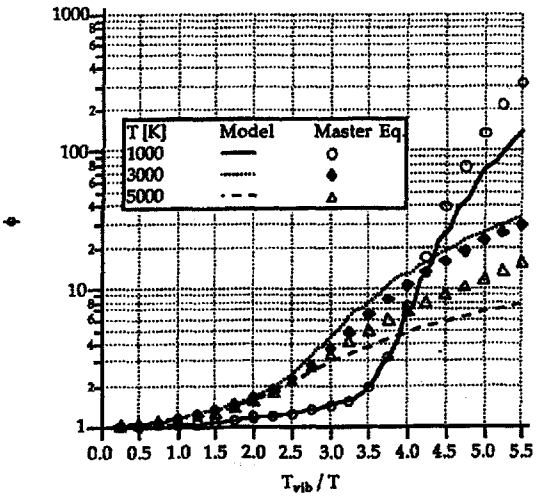

Fig. 3 Comparison of ϕ predicted by Ruffin's simplified anharmonic relaxation model to master equation results for the relaxation of N_2 (Copyright 1994, American Institute of Aeronautics and Astronautics - reprinted with permission from Ref. 24).

Verification

As previously discussed, an effort is currently underway at Sandia National Laboratories to verify the SACCARA compressible fluid mechanics code. The code verification efforts described herein are limited to comparison to an inviscid benchmark solution and code-to-code comparisons. The primary focus of the current section is on the accuracy of the current simulations (i.e. solution verification) with regards to iterative and spatial errors.

Benchmark Inviscid Solution

Inviscid solutions with the SACCARA code were compared with highly accurate finite-difference results reported by Lyubimov and Rusanov[25] for the inviscid flow of a perfect gas ($\gamma = 1.4$) over a spherically-blunted cone with a 10 degree half-angle. This geometry is similar to the JCEAP model geometry but with an infinitely long cone. Results shown in Fig. 4 indicate good agreement between the inviscid SACCARA solution and the benchmark solution at Mach 8, with a maximum difference of 0.8%.

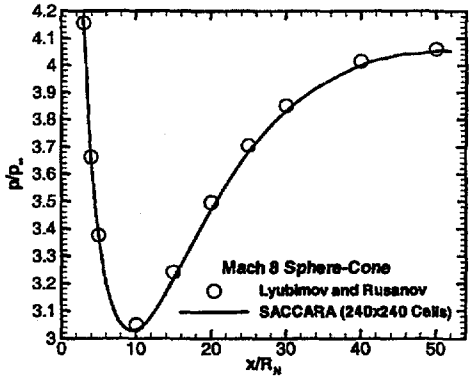

Fig. 4 Comparison of SACCARA pressure distributions with benchmark inviscid solution.[25]

Code-to-Code Comparisons

Code-to-code comparisons have been made using the thin-layer Navier-Stokes code NSEQ[26,27] and the parabolized Navier-Stokes code SPRINT[28,29] to increase the confidence in the SACCARA simulations. The SPRINT code uses NSEQ to provide initial conditions for the space-marching procedure. The results for surface pressure (see Fig. 5) show excellent agreement between the three codes, with maximum differences of less than 0.25%.

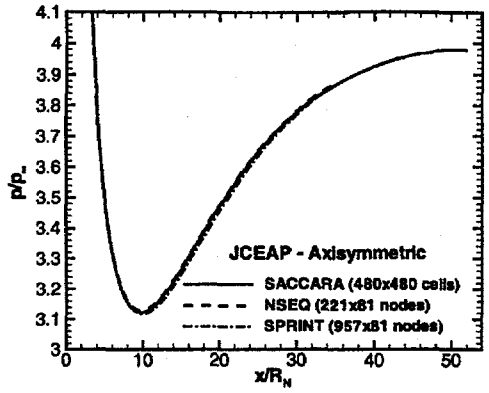

Fig. 5 Code-to-code comparison of SACCARA pressure distributions with NSEQ and SPRINT.

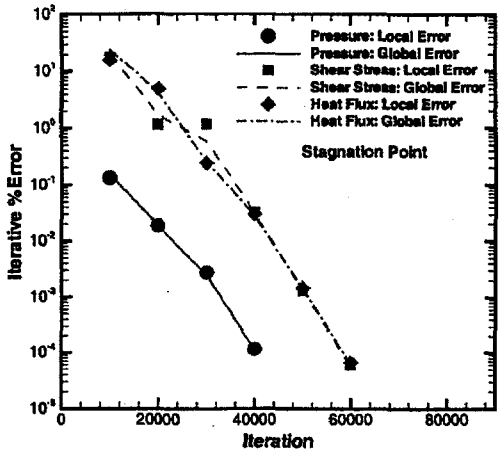

Fig. 6 Iterative convergence error for the 960×960 cell parallel SACCARA simulation (stagnation point).

Iterative Convergence

Iterative convergence was assessed by monitoring the L_2 norms of the residuals for the momentum equations. Since the flowfield is two-dimensional/axisymmetric, laminar, and has no separation or chemical reactions, the residuals were reduced down to machine zero (approximately fourteen orders of magnitude), thus insuring convergence of the iterative algorithm. However, the high computational expense of the finest grid level (960×960 cells) was reduced by restarting from a coarser grid solution (all other simulations were initialized at the freestream conditions) and by carefully monitoring the iterative convergence of the surface properties at two locations. This simulation was run until the iterative errors in surface pressure were reduced below 0.001%.

The method for assessing the iterative convergence of the surface properties is taken from Ref. 30 and provides local estimates of the convergence error based on three sequential iteration levels. The local error estimates for the surface pressure at the stagnation point are presented in Fig. 6 (symbols) along with global estimates (lines). These global values are obtained from the best estimates of the exact solution found by applying the local estimator to the last three iteration levels in the solution. These estimates indicate that the surface pressure converges to within 0.001% accuracy at roughly 32,000 iterations, while the surface shear stress and heat flux (both derivative quantities) require approximately 52,000 iterations. While the required number of iterations appears to be high, the diagonal point-implicit scheme, which has excellent parallel scalability, requires essentially the same computational cost per iteration as an explicit scheme.

The iterative convergence behavior at a location roughly halfway down the body ($x/R_N = 27.2$) is presented in Fig. 7. The surface pressure converges to within 0.02% error much faster (80,000 iterations) than the derivative quantities (150,000 iterations). After 150,000 iterations, the iterative errors in the surface pressure are less than 0.001%. These errors are much smaller than the spatial errors, as will be demonstrated in the following section. The larger number of iterations for this downstream location is indicative of the hyperbolic nature of the problem, where iterative convergence errors in the upstream portions essentially serve as varying boundary conditions for the downstream locations.

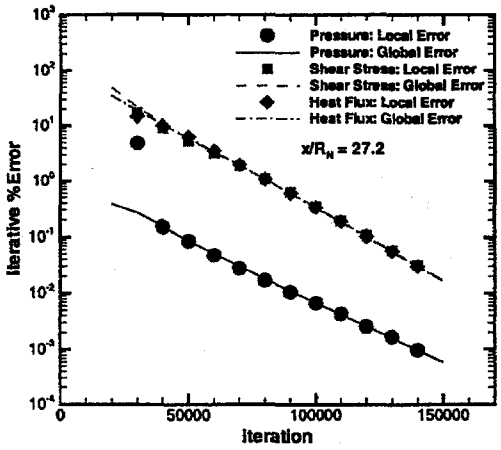

Fig. 7 Iterative convergence error for the 960×960 cell parallel SACCARA simulation ($x/R_N = 27.2$).

Spatial (or Grid) Convergence

Solutions were obtained for seven grid refinement levels, from Mesh 1 (960×960 cells) to Mesh 7 (15×15

cells), with each successive grid level found by eliminating every other grid line in the two spatial dimensions (i.e. grid doubling/halving). More accurate results are obtained by employing Richardson Extrapolation

$$f_{RE} = f_1 + (f_1 - f_2)/3 \tag{5}$$

where f_1 and f_2 are the values on Mesh 1 (960×960) and Mesh 2 (480×480), respectively. This relationship assumes that the numerical scheme is second order accurate and that both grid levels are in the asymptotic grid convergence regime. The surface pressure on the seven grids is presented in Fig. 8 along with the Richardson Extrapolation results. Differences between the finer grid solutions and the extrapolated results are not discernible from the figure.

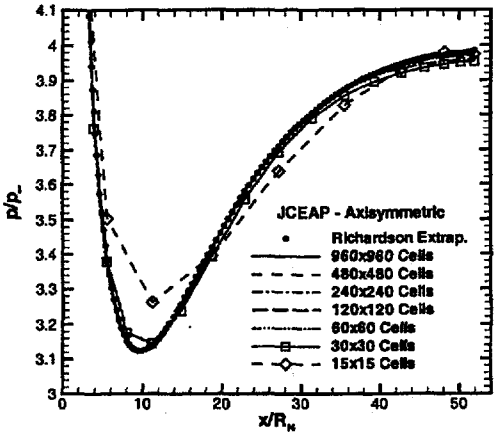

Fig. 8 Surface pressure distributions for the JCEAP simulations using seven mesh levels.

Order of Accuracy

The standard method[31] for determining the spatial order of accuracy of a numerical scheme assumes there is a dominant error term of order p. Using three grid solutions, this order of accuracy can be calculated from the following:

$$p = \ln\left(\frac{f_3 - f_2}{f_2 - f_1}\right) / \ln(r) \tag{6}$$

Eq. (6) requires the assumption of a constant grid refinement factor

$$r = h_3/h_2 = h_2/h_1$$

where h_k represents the grid spacing on mesh k and the subscript 1 denotes the fine mesh solution. This approach assumes that there is a single dominant error term in the three solutions. An example of this procedure is presented in Fig. 9 for the JCEAP surface pressure distributions using the three finest meshes. The solution accuracy varies locally from negative values to values as large as eight. Assessment of the order of accuracy from these types of plots is not possible; in fact, Eq. (6) is undefined when the three pressure solutions are non-monotone (i.e. local maxima or minima exist in the surface pressure versus grid spacing curve). Also shown in the figure are two locations which will be used for additional analysis ($x/R_N = 0$ and $x/R_N = 27.2$).

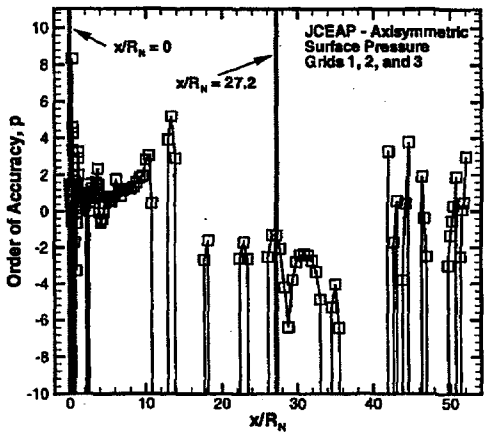

Fig. 9 Order of accuracy of the surface pressure solutions using the three finest meshes.

Insight into the above behavior can be gained by assuming that *both* first and second order error terms are significant. A series representation for the discrete solution[2] on mesh level k is assumed

$$f_k = f_{exact} + g_1 h_k + g_2 h_k^2 + O(h_k^3) \tag{7}$$

which for this case will contain both even and odd error terms since an upwind scheme is used. If three solutions (f_1, f_2, f_3) are known along with the three mesh spacing values (h_1, h_2, h_3), then the three resulting equations form a linear system which may be solved for the first and second order error coefficients (g_1 and g_2) and the third order accurate estimate of the exact solution f_{exact}. The solution to this linear system gives:

$$g_2 = \frac{f_3 - f_2 - r(f_2 - f_1)}{r(r-1)(r^2-1)h_1^2} \tag{8}$$

$$g_1 = \frac{f_3 - f_2 - r^2(r^2-1)g_2 h_1^2}{r(r-1)h_1} \tag{9}$$

$$f_{exact} \cong f_1 - g_1 h_1 - g_2 h_1^2 \tag{10}$$

where again a constant mesh refinement factor r is assumed.

The proposed method has been applied to the surface pressure solutions on the seven mesh levels. Fig. 10 shows the behavior of the error in the surface pressure at the stagnation point. The error is calculated using the

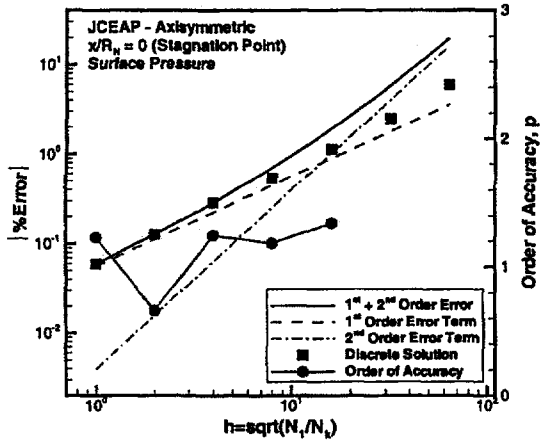

Fig. 10 Magnitude of the error components in surface pressure at $x/R_N = 0$ (stagnation point).

third order accurate estimate for f_{exact} from Eq. (10) above. This error is plotted versus $h = (N_1/N_k)^{1/2}$, where N_1 is the total number of cells on Mesh 1 (the fine mesh) and N_k is the number of cells on Mesh k. Since a grid refinement factor of two (grid halving) was used, the discrete solution points fall at 1, 2, 4, 8, 16, 32, and 64 (from finest to coarsest). Also shown in the figure are the magnitudes of the first and second order error terms

$$\left|\frac{g_1 h}{f_{exact}}\right| \times 100 \quad \text{and} \quad \left|\frac{g_2 h^2}{f_{exact}}\right| \times 100 \tag{11}$$

along with the magnitude of their sum:

$$\left|\frac{g_1 h + g_2 h^2}{f_{exact}}\right| \times 100 \tag{12}$$

The first order error term has a slope of unity on the log-log plot, while the second order error term has a slope of two. The magnitude of the sum of the two terms (solid line) is forced to pass through the points associated with Meshes 1-3 since these solutions are used in the determination of the coefficients in Eqs. (8) and (9). First order accuracy is seen in the fine grid solutions, while the error analysis predicts that the coarse grid solutions will begin to exhibit a second order behavior. Indeed, the coarse grid solutions begin to approach the second order slope. In this case, the first and second order coefficients (g_1 and g_2) have the same sign, so the magnitude of the sum of the error terms is larger than each of the individual error terms. Also shown in the figure is the order of accuracy p as calculated from Eq. (6). For this case, the order of accuracy is well-defined and varies between 0.6 and 1.4.

The error in surface pressure at a location halfway down the body ($x/R_N = 27.2$) is given in Fig. 11. As was seen in Fig. 10, the solutions display first order grid convergence for the finer grids and second order convergence for the coarser grids. This result is consistent with the finding of Ref. 32 where the spatial accuracy of the shock-capturing schemes reverted to first order behind the shock on sufficiently refined meshes. In this case, the first and second order error coefficients are of opposite sign, predicting error cancellation at the cross-over point ($h \approx 7$). The non-monotone behavior predicted from the error analysis (using the three finest mesh solutions only) is qualitatively seen in the discrete solutions on the coarse meshes. The fact that the pressure does not converge monotonically results in singular behavior for the standard method for order of accuracy (also shown in the figure) since the argument of the natural logarithm in Eq. (6) becomes negative.

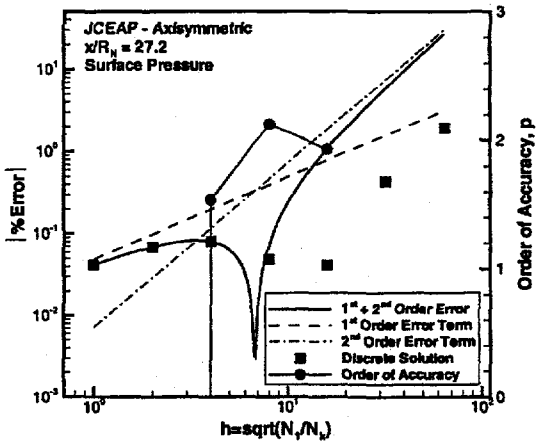

Fig. 11 Magnitude of the error components in surface pressure at $x/R_N = 27.2$.

The assumption that the primary error components are first and second order is supported by the qualitative agreement between the coarse grid error estimates and the discrete errors shown in Figs. 10 and 11. Based on

the above arguments, an alternative method for calculating the order of accuracy is now possible. If the assumption of only first and second order error terms is again made, then the order of accuracy can be expressed as

$$p = 1 + \frac{\left|g_2 h^2\right|}{\left|g_1 h\right| + \left|g_2 h^2\right|} \tag{13}$$

where $\left|g_1 h\right|$ and $\left|g_2 h^2\right|$ are the magnitudes of the first and second order terms, respectively. This expression for p will approach one when the first order error term dominates and two when the second order error term dominates. Since the error coefficients g_1 and g_2 are continuous functions found from the three discrete solutions with grid spacing h_1, h_2, and h_3, it is appropriate to evaluate Eq. (13) at the intermediate mesh level (i.e. set $h = h_2$). Substituting the general form of g_1 and g_2 from Eqs. (8) and (9) into Eq. (13) above and rearranging yields the following expression

$$p = \frac{1}{\varphi + 1} \tag{14}$$

where

$$\varphi = \frac{r+1}{r}\left|\frac{(f_3 - f_2) - r^2(f_2 - f_1)}{(f_3 - f_2) - r(f_2 - f_1)}\right| \tag{15}$$

As a cautionary note, Eq. (15) should only be applied once the first and second order error terms have been demonstrated to be the dominant error terms. The application of this equation to three coarse grid solutions where the higher order error terms dominate will (erroneously) yield an order of accuracy between one and two.

The behavior of this method for estimating the order of accuracy is shown below in Fig. 12 along with the standard method from Eq. (6). The order of accuracy from the alternative method is fairly well behaved and, by construction, will only give results between one and two. Although the order of accuracy p from the current method could be used with a generalized Richardson Extrapolation procedure to obtain an estimate of the exact solution, this value will not be as accurate as the value found from Eq. (10). It should be noted that the preceding analysis is readily extendable to include higher order error terms by simply adding additional mesh levels.

The capturing of discontinuities (e.g. shock waves) without oscillation requires a reduction in the local spatial accuracy of a numerical scheme to first order.[33] For the JCEAP simulations, the first order behavior at the

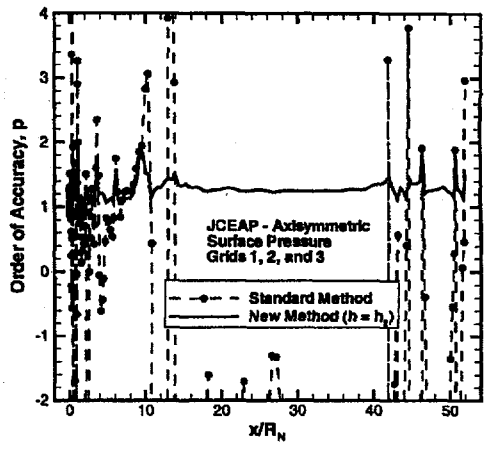

Fig. 12 Order of accuracy of the surface pressure solutions using the three finest meshes.

shock wave leads to the presence of a first order error component (however small) everywhere downstream. As the mesh spacing is refined, this first order error component must eventually dominate. The standard method for assessing the order of spatial accuracy is inadequate when the first and second order error terms are of the same magnitude. In a strict sense, the asymptotic grid convergence regime occurs when there is a single dominant error term as the mesh spacing $h \rightarrow 0$, which for this case is first order. Downstream of the shock wave, the coefficient on the first order error term g_1 is small, with the magnitude possibly related to the proximity to the discontinuity. In these regions, a second order asymptotic region may exist which corresponds to the local truncation error. Once sufficient grid refinement is done, the errors from the discontinuity become significant, thus resulting in a first order asymptotic region. For practical purposes, the second order asymptotic regime should be sufficient for engineering calculations; however, the error and order of accuracy analyses must take into account the fact that both first and second order error terms may be present.

Convergence of the Richardson Extrapolation Estimates

While the standard method for calculating order of accuracy (Eq. (6)) has been shown to be inappropriate for mixed first and second order schemes, it is worthwhile to examine the behavior of the standard Richardson Extrapolation method for estimating the exact solution on the various grid levels. Fig. 13 gives the error in the estimation of the exact stagnation point pressure using second order Richardson Extrapolation (*RE*). Here the percent error is determined by the following relation:

$$\%\text{Error} = \frac{f_{RE} - f_{exact}}{f_{exact}} \times 100 \qquad (16)$$

where f_{exact} is taken to be the third order accurate estimate found from Mesh levels 1 through 3 using Eq. (10). Since Richardson Extrapolation requires two solutions, estimates are only available for the six finest mesh levels (e.g. RE_{34} uses information from Meshes 3 and 4 and is presented at Mesh level 3). While the Richardson Extrapolation estimates improve at $x/R_N = 0$ as the mesh is refined, the error is below 1.5% for all mesh levels.

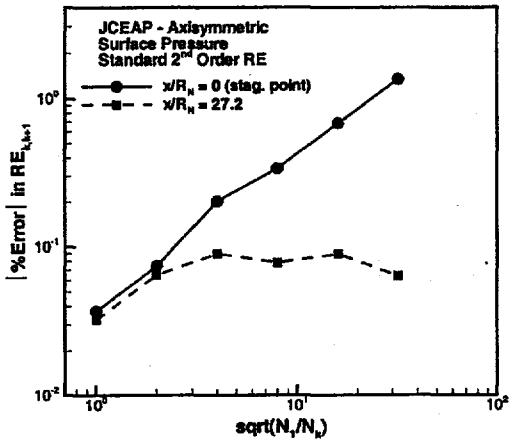

Fig. 13 Error in standard Richardson Extrapolation estimates relative to the third order accurate estimates found from Eq. (10).

Fig. 13 also gives the error in the Richardson Extrapolation estimate for the surface pressure at $x/R_N = 27.2$. While the estimates do not necessarily improve with mesh refinement, the errors are below 0.1% in all cases. These results are encouraging since even though the order of accuracy of the solutions is changing from two to one, the error estimates based on the standard second order Richardson Extrapolation are still surprisingly accurate.

Error Analysis

The error of the pressure solutions relative to the third order accurate estimate from Eq. (10) is presented in Fig. 14. The errors are largest at the sphere cone juncture ($x/R_N \approx 0.83$) and the stagnation point. The errors at these two locations along with the $x/R_N = 27.2$ location are summarized below in Table 2. The large errors at the sphere-cone juncture indicate that additional grid refinement is required at geometric boundaries with discontinuous surface curvature. With the exception of the sphere-cone juncture point, the errors on the three finest

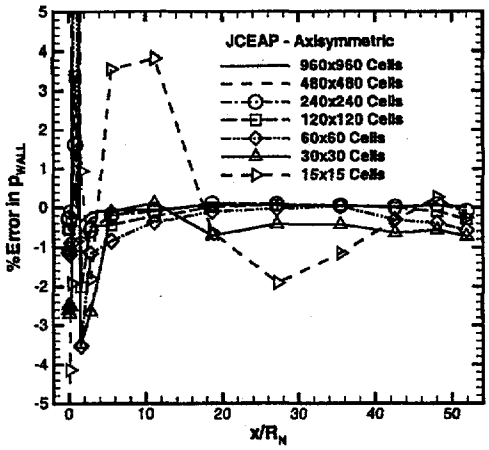

Fig. 14 Error in the surface pressure distributions for the JCEAP simulations using seven mesh levels.

Table 2 Error in surface pressure

Mesh Level	Stagnation Point	Sphere-Cone Juncture	x/R_N=27.2
960×960	-0.060%	0.36%	0.041%
480×480	-0.13%	0.74%	0.068%
240×240	-0.28%	1.6%	0.079%
120×120	-0.54%	3.4%	0.048%
60×60	-1.1%	9.4%	-0.041%
30×30	-2.5%	23.3%	-0.43%
15×15	-5.9%	52.4%	-1.9%

meshes are all below 0.28% and are considered sufficiently small for model validation purposes.

Model Validation

Transport Property Models

A study of the transport properties for nitrogen was undertaken in order to insure accuracy over the temperature range from 50 K to 650 K. Keyes model[34] was chosen for the absolute viscosity (in $N{\cdot}s/m^2$)

$$\mu = \frac{a_0\sqrt{T}}{1 + \dfrac{a}{T \cdot 10^{(a_1/T)}}} \qquad (17)$$

where $a_0 = 1.418\times10^{-6}$, $a = 116.4$, and $a_1 = 5.0$, and was correlated for a range of $90\ K < T < 1695\ K$. Keyes

model is shown in Fig. 15 along with Sutherlands law and experimental data from Refs. 35 and 36. Good agreement with the data is shown for Keyes model from 30 K to 1000 K.

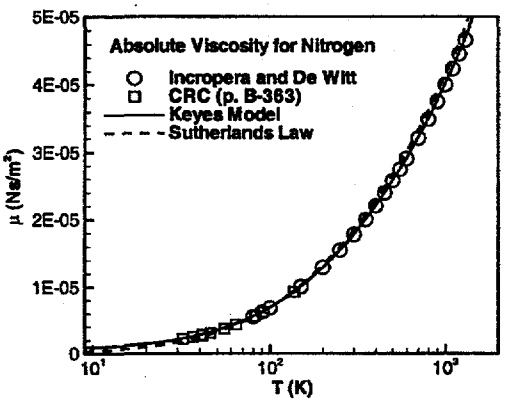

Fig. 15 Absolute viscosity for nitrogen with comparison to experimental data.[35,36]

Keyes model for the thermal conductivity takes the same form as that for the absolute viscosity, however the constants are given as $a_0 = 1.8506\times10^{-3}$, $a = 77.0$, and $a_1 = 12.0$. Using these constants and the form specified in Eq. (17) gives the thermal conductivity, k ($W/m{\cdot}K$), in the range $273\ K < T < 773\ K$. A comparison of Keyes model for thermal conductivity with experimental data[35,36] indicates that the model does not perform well at low temperatures (see Fig. 16). Better agreement with the data is found by simply assuming a constant molecular Prandtl number, $Pr = 0.71$ along with Keyes model for viscosity.

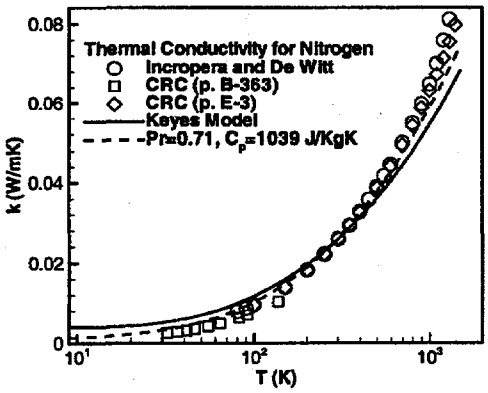

Fig. 16 Thermal conductivity for nitrogen with comparison to experimental data.[35,36]

Equation of State Model

The governing equations are augmented by the standard ideal gas equation of state:

$$p = \rho RT \tag{18}$$

In order to test the validity of this model for the JCEAP simulations, the densities and temperatures from and ideal gas solution were used in an a posteriori calculation of the pressure using the more accurate Beattie-Bridgeman equation of state,[37] which takes into account intermolecular forces. These pressures were then compared to the ideal gas solution results, with differences of less than 0.05% for the entire flowfield.

Thermodynamic Model

Hypersonic Nozzle Calculations

In order to determine the thermal state of the hypersonic wind tunnel (equilibrium versus nonequilibrium), and to assess the flowfield nonuniformity at the test sections, calculations were performed for the Sandia National Laboratories hypersonic wind tunnel Mach 8 nozzle. These calculations employed the second order TVD flux scheme and assumed laminar boundary layers on the wind tunnel walls. The manufacturer's specifications (pre-fabrication) were used for the geometry definition. Post-fabrication inspection of the nozzle throat diameter indicated a diameter of 0.02301 m as compared to 0.02270 m used in the calculations. While this difference is small (1.37%), it could lead to Mach number overpredictions by as much as 0.4% based on a simple inviscid analysis. Two axisymmetric grid levels were employed in order to determine grid independence, with the fine grid having 140×60 cells in the axial and radial directions, respectively (see Fig. 17). The coarse grid was formed by eliminating every other gridline in each direction. The test section is located at approximately $x = 2\ m$.

Vibrational Nonequilibrium

In order to determine the thermal state of the flow at the test section, the nozzle was simulated assuming thermal nonequilibrium using the standard Landau-Teller formulation for vibrational relaxation. Viscous results on two coarse grid levels (see Fig. 18) indicate that the vibrational temperature freezes out at roughly 628 K, very near to the plenum (i.e., stagnation) temperature of 633 K.

In the Flowfield Model section, it was found that for certain expanding flows, relaxation rates could be much larger than those predicted from Landau-Teller theory. In order to estimate the effects of this accelerated relaxation, inviscid calculations were performed assuming

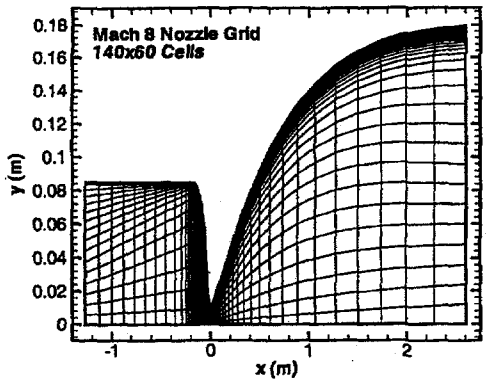

Fig. 17 Viscous nozzle grid (coarsest mesh) for the Mach 8 hypersonic nozzle.

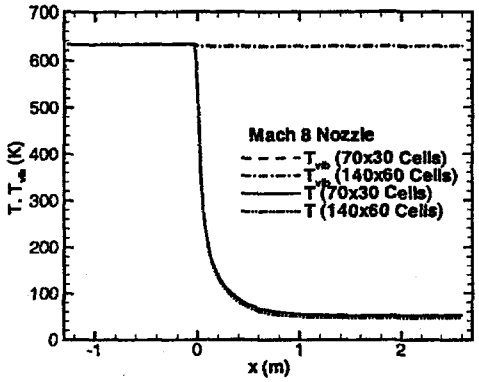

Fig. 18 Temperature profiles in nozzle assuming Landau-Teller relaxation.

the local acceleration factor was globally fixed. While this is certainly not the case (see Fig. 3), this type of analysis is useful to gain qualitative estimates of the true relaxation rates. Fig. 19 gives both translational and vibrational temperatures for acceleration factors between unity (Landau-Teller) and 1×10^6. The results clearly show that large increases in ϕ can affect the relaxation rates near the nozzle throat ($x = 0$); however, these results also show that, due to rapid expansion in the diverging section of the nozzle, the vibrational temperature freezes out very near the throat, regardless of the value of ϕ. A magnified view is presented in Fig. 20, which indicates that vibrational freezing occurs by the $x = 0.1\ m$ location. As shown in Fig. 3, the local acceleration factor is greater than ten only for T_{vib}/T ratios greater than four; however, according to the $\phi = 1$ curve, the T_{vib}/T value at $x = 0.1\ m$ is approximately

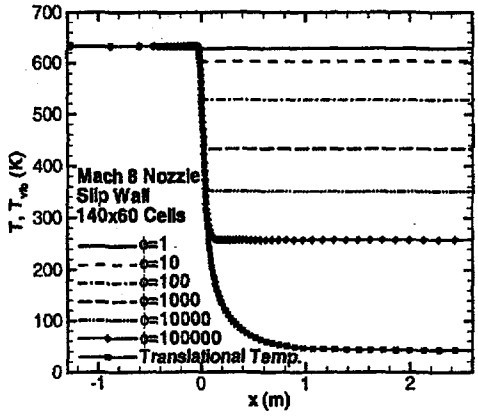

Fig. 19 Vibrational temperature in nozzle for a number of different L-T acceleration factors ϕ (140×60 cells).

three, and even smaller at the upstream locations. Thus, the profile most likely to be representative of the true behavior of the vibrational state should lie somewhere between the $\phi = 1$ and the $\phi = 10$ curves. It should be noted that this argument assumes that the local acceleration factor for this case is of approximately the same shape as the $T = 1000\ K$ profile given in Fig. 3. An analysis by Ruffin[38] using the simplified anharmonic relaxation model on a similar nozzle geometry provides further evidence of rapid vibrational freezing in the nozzle.

Nonequilibrium Effects on Freestream Mach Number

Based on the above arguments for vibrationally frozen flow in the tunnel, the assumption of equilibrium

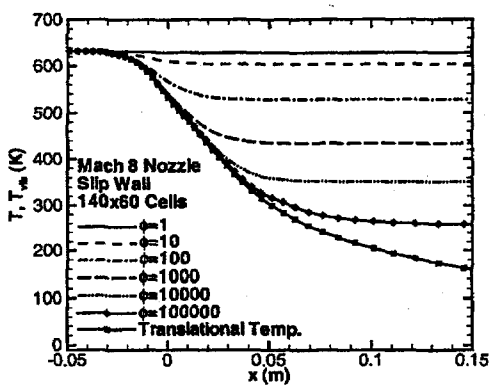

Fig. 20 Enlarged view of the vibrational temperature in nozzle for a number of different L-T acceleration factors ϕ (140×60 cells).

theory used in the experimental Mach number calibration is not valid. Furthermore, simulations on the JCEAP geometry indicate that the freestream pressure at the test section is low enough that, even through the normal shock wave, the flow remains thermally frozen until it reaches the wall boundary layer. Calculations of the Mach number from measured stagnation and pitot pressures show that assuming frozen flow yields a Mach number approximately 0.23% lower than that found from equilibrium theory. This difference, although small, represents a bias error in the calibration of freestream Mach number. Errors of this order can adversely affect validation efforts, especially for the current case, where agreement between computations and experiment is desired within a few percent.

These differences in the Mach number based on frozen flow (nonequilibrium) versus equilibrium theory arise due to the dependence of the Mach number on the ratio of specific heats γ when establishing isentropic and normal shock relations. Although very little energy is tied up in the vibrational modes at $T_{vib} = 628\ K$, the effect on gamma can have an impact on the determination of freestream conditions.

Nonequilibrium Effects on JCEAP Simulations

Although not shown, simulation results assuming thermal nonequilibrium and thermal equilibrium gave no differences in surface pressure. This lack of sensitivity indicates that the nonequilibrium effects discussed previously impact the simulation results primarily through the freestream boundary conditions (Mach number, pressure, etc.).

Continuum Flow Assumption

In order to insure that the assumption of continuum flow is valid for the wind tunnel nozzle in the low-pressure rapid expansion region, the continuum breakdown parameter P was calculated.[39] Continuum theory breaks down for $P > 0.02$, and the maximum values calculated in the Mach 8 nozzle simulations were approximately 2×10^{-5}, thus confirming the use of continuum theory.

Uniform Flow Assumption

From the laminar nozzle calculations, estimates of the spatial nonuniformity due to axisymmetric waves in the nozzle can be made. In the experiment, two test section locations were used in order to minimize the effects of these tunnel flow nonuniformities. Mach number and pressure across the two test sections (corresponding to model nosetip locations) are given in Fig. 21. For reference, the model base radius (approximately 0.051 m) is also shown. Mach number variations in the region corresponding to the model base are less than 0.1%, while

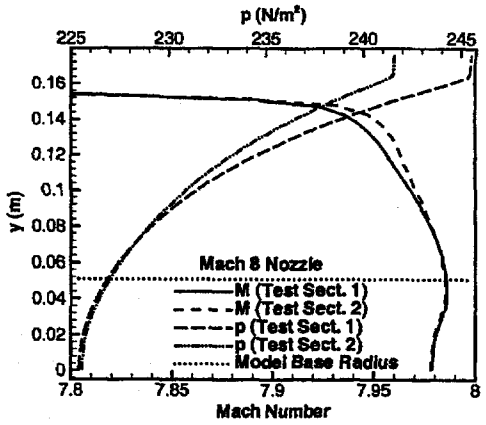

Fig. 21 Mach number and pressure profiles across the two test section locations.

pressure variations are as large as 0.65%. The temperature and density are given in Fig. 22, with maximum variations over the effective model cross-section of 0.16% and 0.81%, respectively. The variations in pressure and density were included in the simulation boundary conditions by using the reported freestream values at the centerline and allowing the radial distribution to change according to Figs. 21 and 22; however, negligible differences in the surface pressures were found.

It should be noted that the preceding analysis accounts only for the effects of axisymmetric waves on the flowfield nonuniformity. This analysis omits nonuniformities due to the rectangular-to-axisymmetric transition (which occurs approximately 0.1 m upstream of the nozzle throat), flow obstructions upstream of the plenum (e.g. heater screens), or asymmetries in the tunnel manufacture and assembly. The proper way to include these effects is to perform a detailed measurement of the flow

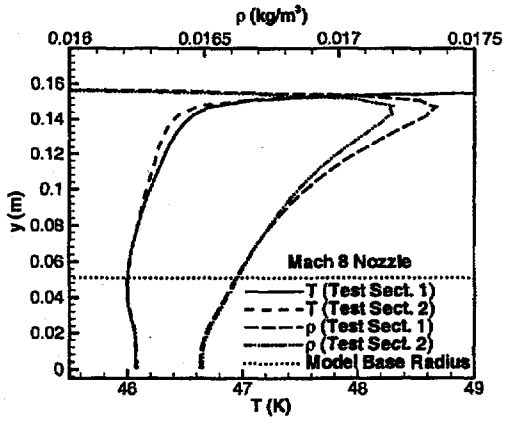

Fig. 22 Temperature and density profiles across the two test section locations.

properties (velocity components, pressure, temperature) at some location upstream of the test section to be used as an inflow boundary condition for the computations.

Base Flow Model

For all the simulations presented herein, a supersonic outflow condition was applied at the outflow boundary (i.e. the end of the vehicle). This boundary condition is clearly not appropriate in the subsonic portion of the boundary layer where information can travel upstream. In order to assess the effects of this boundary condition on the pressure distributions, an axisymmetric case was run which included the base region. While the model is only 0.264 *m* long, the domain had to be extended to 2.5 *m* in the axial direction to insure supersonic flow in the wake region. The wake was assumed to be laminar, and a supersonic recirculation zone appears consistent with earlier laminar computational studies.[40] The forebody grid used 250×240 cells and was essentially the 240×240 axisymmetric grid with clustering to the end of the model. The base region has 340×360 cells with clustering to the base region and the shear layer. The computations were run in parallel on six processors of the Sun Enterprise 10000 shared-memory machine.

While the pressure does drop dramatically near the base (as shown in Fig. 23), the upstream influence is only seen for $2.5R_N$ upstream (approximately four boundary layer thicknesses). Thus, while the presence of the base flow does affect the pressure at the corner, the upstream effects are limited and will not affect the experimental data comparisons since the farthest aft data location is at $x/R_N \approx 46.5$.

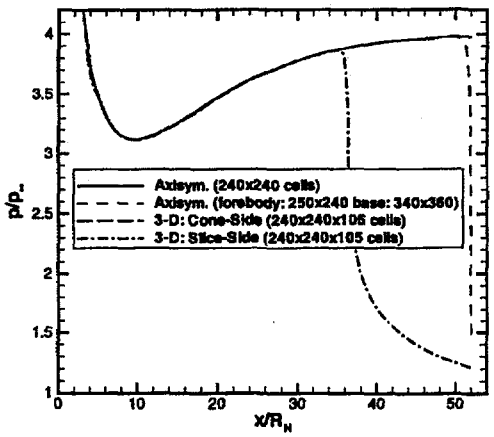

Fig. 23 Comparison of baseline simulation results with axisymmetric calculation including base flow and full three dimensional simulation including the planar slice.

Axisymmetric Flow Assumption

The appropriateness of the axisymmetric flow assumption was addressed by conducting full three dimensional calculations of the JCEAP geometry including the planar slice on the aft end of the model but without the flaps (see Fig. 1). A symmetry plane was assumed, thus only half of the model was simulated. The three dimensional grid was based on the 240×240 axisymmetric grid (considered the coarsest grid accurate enough for experimental data comparisons) and employed 105 azimuthal grid cells from the cone-symmetry plane to the slice-symmetry plane (180 degrees). The grid was decomposed into 144 zones (as shown in Fig. 24) and run in parallel on the ASCI Red Teraflops machine. With the exception of the planar slice region, little effect is seen in the upstream region and on the cone-side (see Fig. 23). Maximum differences between the baseline axisymmetric simulation and the three dimensional calculations are approximately 0.25%.

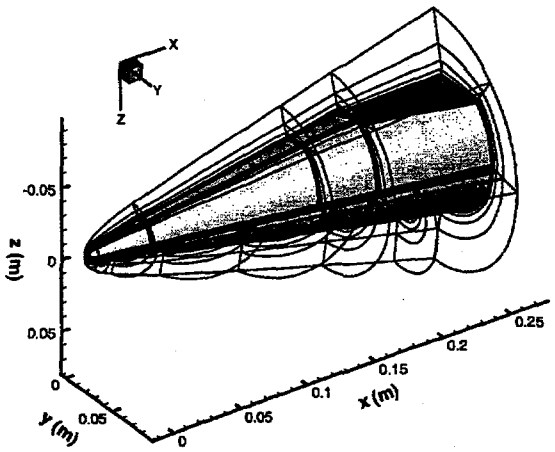

Fig. 24 Three dimensional JCEAP grid with 240×240×105 mesh cells and 144 zones.

Surface Pressure Predictions

In order to validate the SACCARA code for laminar, hypersonic flows, comparisons were made to the experimental surface pressure data from the JCEAP experiment.[10,11] As previously mentioned, the actual JCEAP geometry has a planar slice on the aft portion of the model. While comparisons of axisymmetric computational results with data on the slice are clearly not appropriate, the findings from the preceding subsections indicate that the data on the conical portions of the model (cone-side and slice-side upstream of the slice) can be used to validate the axisymmetric simulations.

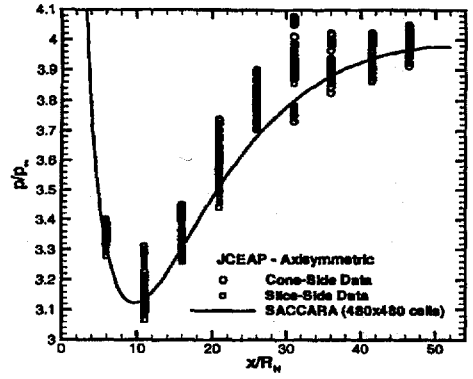

Fig. 25 Comparison of the SACCARA surface pressure results with the JCEAP data (all data points shown).

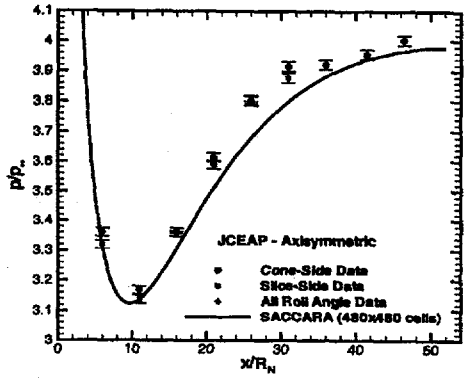

Fig. 26 Comparison of the SACCARA surface pressure results with mean JCEAP data.

Surface pressure distributions are compared with experimental data in Fig. 25 with all data points shown. The scatter in the data indicates the presence of random error and correlated bias error as discussed in Refs. 8 and 10. A large number of runs were conducted at different roll angles and at the different axial stations. Statistical procedures were then applied to determine error bounds.[10] Comparison to the data with 95% (2σ) confidence bands is shown in Fig. 26. The computed pressure ratios fall consistently below the experimental data, with the poorest agreement occurring upstream of the slice location (x/R_N = 21, 26, and 31). The maximum difference, occurring at the x/R_N = 26 location, is 3.3%, well outside the experimental 2σ error bound of ±0.4 %. Based on the verification evidence presented in the previous sub-section, the lack of agreement between the simulation and the experiment is due to either a poor characterization of the tunnel conditions (used for simulation boundary conditions) or a bias error in the experimental data.

Although the accuracy of the three dimensional simulations has not been verified, the 240×240 cell axisymmetric mesh was used as a baseline in generating the three dimensional grid (240×240×105 cells). Based on the experience with the error analysis on the axisymmetric grids and the favorable comparison of the cone-side surface pressure between the axisymmetric and three dimensional calculations, it may be useful to compare the three dimensional simulation with the slice-side experimental data. This comparison is given in Fig. 27 and shows very good agreement between the calculations and the data on the slice; however, further work needs to be done to verify the accuracy of the three dimensional calculation.

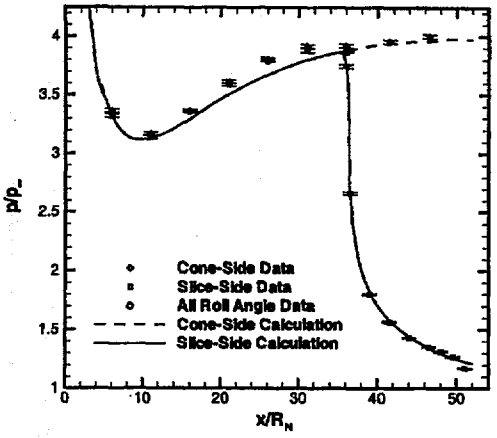

Fig. 27 Comparison of the three dimensional SACCARA surface pressures with mean JCEAP data.

Bias Errors

From the hypersonic wind tunnel simulations (discussed in the Thermodynamic Models validation subsection), it was found that the assumption of thermal equilibrium in the experimental Mach number calibration was not valid. Based on the experimentally measured values for stagnation pressure in the plenum and pitot pressure in the test section, a more physically consistent value for the freestream Mach number was calculated by assuming frozen flow with an appropriate value of gamma (γ = 1.4). Using the standard isentropic and normal shock relations for a calorically perfect gas, a nonlinear equation for Mach number was obtained as a function of these two pressures. This method resulted in a freestream Mach number of 7.823, 0.23% lower than

the experimentally reported value of 7.841 which comes from the thermal equilibrium assumption. Based on a simple oblique shock wave analysis with a shock angle of 12 degrees (determined from the simulations), the 0.23% reduction in Mach number corresponds to a 0.5% reduction in the simulation pressure ratio. However, this bias error does not explain the differences seen between the simulation results and the experimental surface pressure data.

Another potential source of bias error is the averaging of the pitot pressures across the entire test section to determine the freestream Mach number. The pitot rake used in the Mach number calibrations has probes spaced 0.0572 *m* (2.25 *in*) apart. The region which can influence the surface pressures for the Mach 8 flow is roughly on the order of the base radius of 0.0508 *m* (2 *in*). Therefore, one could argue that rather than using an average of the seven probes (two as far as 0.1143 *m* away), it is more appropriate to use the centerline probe only to calculate the freestream Mach number. By examining the actual Mach number calibration data, the centerline probe was found to give a Mach number approximately 0.6% larger than the averaged value. This represents a potential bias error in the freestream Mach number. Including this bias error would increase the freestream Mach number from the reported value of 7.841 to a value of 7.887. Again employing the oblique shock analysis, the 0.6% increase in Mach number corresponds to a 1.3% increase in the simulation pressure ratio. Some other possible sources of experimental bias errors include the difficulty in achieving a reference pressure well below the low tunnel static pressures and errors in the standard used to calibrate the pressure transducers.

Concluding Remarks

Simulations have been conducted for the laminar, perfect gas flow over a 10 degree half-angle sphere-cone. The accuracy of the pressure predictions have been verified to within approximately 0.1% by carefully monitoring iterative and grid convergence. Additional confidence in the simulations was gained by comparing inviscid results to a highly-accurate benchmark solution and by performing code-to-code comparisons.

In general, numerical schemes reduce to first order accuracy through discontinuities such as shock waves to prevent oscillations. The first order behavior at the shock wave leads to the presence of a first order error component (however small) everywhere downstream. As the mesh spacing is refined, this first order error component will eventually dominate. The standard method for assessing the order of spatial accuracy was shown to be inadequate when the first and second order error terms are of similar magnitude. An alternative method was proposed for analyzing both the convergence behavior and order of accuracy for mixed first and second order schemes.

The computational submodels for the transport properties, equation of state, thermodynamic state, and the base-flow boundary condition were validated. In addition, the assumptions made in the computations regarding continuum flow, uniform freestream conditions, and axisymmetric flow were found to be valid. While the Mach number calibration in the experiment assumed thermal equilibrium, simulations of the hypersonic wind tunnel nozzle found the flow to be thermally frozen. Bias errors from assuming equilibrium theory would reduce the freestream Mach number by 0.23%. Bias errors in the tunnel Mach number calibration related to the averaging of the pitot probe readings across the entire test section were discussed. Accounting for this potential bias error would increase the freestream Mach number by an estimated 0.6%. After accounting for these experimental bias errors, the maximum difference between the data and the simulation results for surface pressure are within 2.5%. This difference is still well outside the experimental 2σ error bounds of ± 0.4 %.

It is difficult to resolve these inconsistencies due to the time span (approximately five years) between the experiment and the current computations. Thus it is clear that validation experiments must be carried out in conjunction with computational analyses. Not only would this aid in design of the experiment, but it would provide an additional check on the assumptions made, both in the experiment and in the computations.

A recalibration of the freestream parameters used in the experiment and the data reduction is needed. This recalibration should use frozen flow theory instead of assuming the flow is in thermal equilibrium, and should have finer spatial resolution to provide detailed boundary conditions to be used as inflow conditions for modeling and simulation. Finally, the experimental database should be further investigated for the possibility of bias errors in the measurements and the data reduction process. Once the discrepancies between the experimental data and the simulation results are resolved, data comparisons can be made at various angles of attack and flap deflection angles. This hierarchy of physical complexity in validation experiments demonstrates the synergism between computation and experiment that can be achieved.

Acknowledgments

The authors would like to thank Jeff Payne of Sandia National Laboratories for the many discussions on computational fluid dynamics and for his help with the three dimensional calculations. We would like to thank Fred

Blottner of Sandia National Laboratories for his help in the area of solution accuracy assessment. Thanks also go to Dan Aeschliman who, along will Bill Oberkampf, provided the experimental data. Finally, we would like to thank Professor Stephen Ruffin of the Georgia Institute of Technology for his consultations regarding vibrational nonequilibrium. This work was supported by Sandia National Laboratories and the Department of Energy's Accelerated Strategic Computing Initiative.

References

1. *Guide for the Verification and Validation of Computational Fluid Dynamics Simulations*, AIAA G-077-1998, p. 3.

2. Roache, P. J., "Ch. 3: A Methodology for Accuracy Verification of Codes: the Method of Manufactured Solutions," *Verification and Validation in Computational Science and Engineering*, Hermosa Publishers, New Mexico, 1998.

3. Wong, C. C., Soetrisno, M., Blottner, F. G., Imlay, S. T., and Payne, J. L., "PINCA: A Scalable Parallel Program for Compressible Gas Dynamics with Nonequilibrium Chemistry," SAND 94-2436, Sandia National Laboratories, Albuquerque, NM, 1995.

4. Wong, C. C., Blottner, F. G., Payne, J. L., and Soetrisno, M., "Implementation of a Parallel Algorithm for Thermo-Chemical Nonequilibrium Flow Solutions," AIAA Paper 95-0152, Jan. 1995.

5. B. Hassan, D. W. Kuntz, and D. L. Potter, "Coupled Fluid/Thermal Prediction of Ablating Hypersonic Vehicles," AIAA Paper No. 98-0168, Jan. 1998.

6. D. W. Kuntz, B. Hassan, and D. L. Potter, "An Iterative Approach for Coupling Fluid/Thermal Predictions of Ablating Hypersonic Vehicles," AIAA Paper 99-3460, June-July 1999.

7. INCA User's Manual, Version 2.0, Amtec Engineering, Inc., Bellevue, WA, 1995.

8. Oberkampf, W. L., Aeschliman, D. P., Tate, R. E., and Henfling, J. F., "Experimental Aerodynamic Research on a Hypersonic Vehicle," SAND 92-1411, Sandia National Laboratories, Albuquerque, NM, 1993.

9. Oberkampf, W. L., and Aeschliman, D. P., "Joint Computational/Experimental Aerodynamics Research on a Hypersonic Vehicle, Part 1: Experimental Results," *AIAA Journal*, Vol. 9, No. 3, 1995, pp. 432-437.

10. Oberkampf, W. L., Aeschliman, D. P., Henfling, J. F., and Larson, D. E., "Surface Pressure Measurements for CFD Code Validation in Hypersonic Flow," AIAA Paper 95-2273, June 1995.

11. Oberkampf, W. L., Aeschliman, D. P., Henfling, J. F., Larson, D. E., and Payne, J. L., "Surface Pressure Measurements on a Hypersonic Vehicle," AIAA Paper 96-0669, Jan. 1996.

12. Yoon, S., and Jameson, A., "An LU-SSOR Scheme for the Euler and Navier-Stokes Equations," AIAA Paper 87-0600, Jan. 1988.

13. Yoon, S., and Kwak, D., "Artificial Dissipation Models for Hypersonic External Flow," AIAA Paper 88-3708, 1988.

14. Peery, K. M., and Imlay, S. T., "An Efficient Implicit Method for Solving Viscous Multi-Stream Nozzle/Afterbody Flow Fields," AIAA Paper 86-1380, June 1986.

15. Payne, J. L., and Hassan, B., "Massively Parallel Computational Fluid Dynamics Calculations for Aerodynamics and Aerothermodynamics Applications," Proceedings of the 1998 HPCCP/CAS Workshop, NASA/CP-1999-208757, Jan. 1999, pp. 111-116.

16. Steger, J. L., and Warming, R. F., "Flux Vector Splitting of the Inviscid Gasdynamic Equations with Applications to Finite Difference Methods," *Journal of Computational Physics*, Vol. 40, 1981, pp. 263-293.

17. Walker, M. M., and Oberkampf, W. L., "Joint Computational/Experimental Aerodynamics Research on a Hypersonic Vehicle, Part 2: Computational Results," *AIAA Journal*, Vol. 30, No. 8, 1992, pp. 2010-2016.

18. Yee, H. C., "Implicit and Symmetric Shock Capturing Schemes," NASA TM-89464, May 1987.

19. McBride, B. J., Gordon, S., and Reno, M. A., "Coefficients for Calculating Thermodynamic and Transport Properties of Individual Species," NASA TM 4513, Oct. 1993.

20. Gnoffo, P. A., Gupta, R. N., and Shinn, J. L., "Conservation Equations and Physical Models for Hypersonic Air Flows in Thermal and Chemical Nonequilibrium," NASA TP-2867, Feb. 1989.

21. Millikan, R. C., and White, D. R., "Systematics of Vibrational Relaxation," *Journal of Chemical Physics*, Vol. 39, No. 12, 1963, pp. 3209-3213.

22. Bray, K. N. C., "Chemical and Vibrational Nonequilibrium in Nozzle Flows," *Nonequilibrium Flows, Part II*, Marcel Dekker, Inc., New York, 1970, pp. 67-68.

23. Ruffin, S. M., "Prediction of Vibrational Relaxation in Hypersonic Expanding Flows Part 1: Model Development," *Journal of Thermophysics and Heat Transfer*, Vol. 9, No. 3, 1995, pp. 432-437.

24. Ruffin, S. M., "Prediction of Vibrational Relaxation in Hypersonic Expanding Flows Part 2: Results," *Journal of Thermophysics and Heat Transfer*, Vol. 9, No. 3, 1995, pp. 438-445.

25. Lyubimov, A. N., and Rusanov, V. V., "Gas Flows Past Blunt Bodies, Part II: Tables of the Gasdynamic Functions," NASA TT F-715, Feb. 1973.

26. Blottner, F. G., and Larson, D. E., "Navier-Stokes Code NS3D for Blunt Bodies, Part I: Analysis, Results, and Verification," SAND 88-0504/1, Sandia National Laboratories, Albuquerque, NM, 1988.

27. Blottner, F. G., "Accurate Navier-Stokes Results for the Hypersonic Flow over a Spherical Nosetip," *Journal of Spacecraft and Rockets*, Vol. 27, No. 2, 1990, pp. 113-122.

28. Walker, M. A., "SPRINTRUN: A User Friendly Input Processor for the SPRINT Code," SAND 89-

0625, Sandia National Laboratories, Albuquerque, NM, 1990.

29. Stalnaker, J. F., Nicholson, L. A., Hanline, D. S., and McGraw, E. H., "Improvements to the AFWAL Parabolized Navier-Stokes Code Formulation," Air Force Wright Aeronautical Lab., TR-86-3076, Wright-Patterson AFB, Dayton, OH, Sept. 1986.

30. Roy, C. J., and Blottner, F. G., "Assessment of One- and Two-Equation Turbulence Models for Hypersonic Transitional Flows," AIAA Paper 2000-0132, January 2000.

31. de Vahl Davis, G., "Natural Convection of Air in a Square Cavity: A Bench Mark Numerical Solution," *International Journal for Numerical Methods in Fluids*, Vol. 3, No. 3, 1983, pp. 249-264.

32. Carpenter, M. H., and Casper, J. H., "Accuracy of Shock Capturing in Two Spatial Dimensions," *AIAA Journal*, Vol. 37, No. 9, 1999, pp. 1072-1079.

33. Van Leer, B., "Towards the Ultimate Conservative Difference Scheme. I. The Quest of Monotonicity," *Lecture Notes in Physics*, Vol. 18, Springer Verlag, Berlin, 1973, pp. 163-168.

34. Keyes, F. G., "A Summary of Viscosity and Heat-Conduction Data for He, A, H_2, O_2, CO, CO_2, H_2O, and Air," Transactions of the ASME, July 1951, pp. 589-596.

35. Incropera, F. P., and DeWitt, D. P., *Fundamentals of Heat and Mass Transfer, 3rd Ed.*, Wiley, New York, 1990, p. A18.

36. *CRC Handbook of Chemistry and Physics*, Robert C. Weast, Editor, CRC Press, Florida, 1984, pp. B-363 and E-3.

37. Cengel, Y. A., and Boles, M. A., *Thermodynamics: an Engineering Approach, 2nd Ed.*, McGraw-Hill, New York, 1994, p. 915.

38. Ruffin, S. M., Personal Communications, September, 1999.

39. Bird, G. A., *Molecular Gas Dynamics and the Direct Simulation of Gas Flows*, Clarendon Press, Oxford, 1994, p. 4.

40. Grasso, F., and Pettinelli, C., "Analysis of Laminar Near-Wake Hypersonic Flows," *Journal of Spacecraft and Rockets*, Vol. 32, No. 6, 1995, pp. 970-980.